

The Alaric parton shower for hadron colliders

Stefan Höche,¹ Frank Krauss,² and Daniel Reichelt²

¹*Fermi National Accelerator Laboratory, Batavia, IL, 60510, USA*

²*Institute for Particle Physics Phenomenology, Durham University, Durham DH1 3LE, UK*

We introduce the ALARIC parton shower for simulating QCD radiation at hadron colliders and present numerical results from an implementation in the event generator SHERPA. ALARIC provides a consistent framework to quantify certain systematic uncertainties which cannot be eliminated by comparing the parton shower with analytic resummation. In particular, it allows to study recoil effects away from the soft and collinear limits without the need to change the evolution variable or the splitting functions. We assess the performance of ALARIC in Drell-Yan lepton pair and QCD jet production, and present the first multi-jet merging for the new algorithm.

I. INTRODUCTION

Experiments at high-energy hadron colliders such as the CERN Large Hadron Collider (LHC) have been the source of much of our understanding of the smallest building blocks of matter. While they often do not reach the same precision as lepton colliders, proton-(anti)proton machines offer unprecedented reach in available center-of-mass energy, and thus open a pathway to the observation of hitherto unknown particles as well as new interactions [1–3]. Quite naturally, opportunity comes at a cost. The composite nature of the beam particles, and the complex phenomenology of QCD at low and high scales hinder the extraction of rare hadron-level signals from large and often poorly understood backgrounds. Computer simulations in the form of Monte-Carlo event generators have so far proven the only effective approach to this problem [4, 5]. Among the many components of these event generators, the approximation of QCD radiative corrections to all orders in perturbation theory is one of the most important. This component is implemented by parton showers.

The discovery of the gluon at PETRA about forty years ago spurred the development of the first parton showers [6–9]. Since then, the increasing center-of-mass energy of the experiments mandated a corresponding increase in precision of the simulations, which led to the development of spin correlation algorithms [10–13], matching to next-to-leading order fixed-order calculations [14–20] and the merging of calculations for varying jet multiplicity [21–31]. Color coherent parton evolution, manifesting itself through angular ordering for global observables [32–37], became a guiding principle for the construction of many early parton shower algorithms [38, 39] and remains a powerful computational tool. However, for observables sensitive to certain correlations among partons and jets, angular ordering does not capture all details of QCD radiative effects [40]. This class of observables can be better described by algorithms based on the color dipole picture, first proposed and implemented in [41–43], and later extended to a more efficient and precise simulation framework [44–48]. Algorithms based on the dipole picture were also supplemented by a matching to single parton evolution in the collinear limit [49–55]. Most parton showers currently used by the LHC experiments are based on this paradigm [5]. Recently, they have again been revised, in order to achieve consistency with analytic resummation in the limit of large center-of-mass energies [56]. The resulting improvements concern kinematic recoil effects [57–65], and an improved simulation of color coherence [44, 66–79].

In this publication we will report on the extension of one of the new dipole-like parton shower algorithms, called ALARIC [63, 64], to initial-state radiation. A unique aspect of the ALARIC method is the non-trivial dependence of splitting functions on the azimuthal emission angle, even when spin correlations are not included. This allows to simulate the complete one-loop soft radiation pattern without the need for angular ordering. At the same time, the choice of recoil momentum necessary to implement four-momentum conservation and on-shell conditions is left arbitrary, enabling an easy matching of the parton-shower to analytic calculations for specific observables. The new method satisfies the stringent criteria for next-to-leading logarithmic (NLL) precision at leading color [56] for all recursively infrared safe observables [63]. Here we will discuss specifically the treatment of the collinear splitting functions in the context of different kinematics mappings, focusing on terms which are not determined by the matching to a soft eikonal. Sub-leading power corrections to these terms vanish in the NLL limit, but can play a significant role at finite transverse momentum [80] and must therefore be implemented as faithful as possible. They are often important at hadron colliders due to the enhanced gluon distribution at high energies and small x [81, 82].

The manuscript is structured as follows. Section II introduces the collinear splitting functions and presents a kinematics-independent definition of the purely collinear terms for final- and initial-state evolution. Section III introduces the kinematic mappings used in our algorithm and discusses an extension of the proposal in Ref. [63]. Section VI presents some first example phenomenological predictions in comparison to experimental data from the Large Hadron Collider. Finally, Sec. VII discusses further directions of development.

II. SPLITTING FUNCTIONS

The precise form of the splitting functions is one of the main systematic uncertainties in any parton-shower simulation. Stringent criteria exist only for the leading terms in gluon energy in the soft gluon limit, and for the leading terms in transverse momentum in the collinear limit. These terms are determined by the known soft [83] and collinear [84–89] factorization properties of QCD amplitudes. It is often assumed that away from the limits, the splitting function can be used as is, without the need to account for the precise definition of the splitting variable. While it is certainly true that changes in its definition only induce sub-leading corrections (of higher power in the soft or collinear expansion parameter), the precise definition of the splitting kernels plays an important role and can be used to capture non-leading effects. A prominent example is the sub-leading power correction to the soft splitting function [90–92], which originates in classical radiative effects [93] and extends the naive soft limit to a physically more meaningful result. Corrections of this type should clearly be included due to their importance for the physics performance of the Monte-Carlo simulation. A similarly important point is that the collinear splitting functions can be computed as off-shell matrix elements in a physical gauge [94], which implies that they contain information on the structure of QCD amplitudes beyond the collinear limit. If this structure is to be retained, it is necessary that the splitting functions be evaluated with the exact same definition of splitting variable that was used in their derivation. A change in the kinematics parametrization must lead to identical physics predictions, but it may require a different form of the splitting functions, including power suppressed terms. In the following, we will recall how to derive the collinear splitting functions, using the algorithm of [94]. In Secs. III A and III B we will then determine their correct arguments in terms of the kinematical parameters used in the parton-shower.

A. Purely collinear splitting functions

If two partons, i and j , of an n -parton QCD amplitude become collinear, the squared amplitude factorizes as

$${}_n\langle 1, \dots, n | 1, \dots, n \rangle_n = \sum_{\lambda, \lambda' = \pm} {}_{n-1}\langle 1, \dots, \check{\lambda}(ij), \dots, \check{\lambda}, \dots, n | \frac{8\pi\alpha_s P_{(ij)i}^{\lambda\lambda'}(z)}{2p_i p_j} | 1, \dots, \check{\lambda}(ij), \dots, \check{\lambda}, \dots, n \rangle_{n-1}, \quad (1)$$

where the notation $\check{\lambda}$ indicates that parton i is removed from the original amplitude, and where (ij) is the progenitor of partons i and j . The $P_{ab}^{\lambda\lambda'}(z)$ are the spin-dependent DGLAP splitting functions, which depend on the momentum fraction z of parton i with respect to the mother parton, (ij) , and on the helicities λ [84–89].

These splitting functions can be derived using the following Sudakov parametrization of the momenta of the splitting products

$$p_i^\mu = z_i \hat{p}_{ij}^\mu + \frac{-k_t^2}{z_i 2p_{ij} \bar{n}} \bar{n}^\mu + k_t^\mu, \quad p_j^\mu = z_j \hat{p}_{ij}^\mu + \frac{-k_t^2}{z_j 2p_{ij} \bar{n}} \bar{n}^\mu - k_t^\mu. \quad (2)$$

In this context, $\hat{p}_{ij}^\mu = p_{ij}^\mu - p_{ij}^2/(2p_{ij} \bar{n}) \bar{n}^\mu$, and \bar{n}^μ is a light-like auxiliary vector, linearly independent of \hat{p}_{ij}^μ and k_t^μ . Equation (2) implies that we can compute the light-cone momentum fractions, z_i and z_j as

$$z_i = \frac{p_i \bar{n}}{p_{ij} \bar{n}}, \quad \text{and} \quad z_j = \frac{p_j \bar{n}}{p_{ij} \bar{n}}. \quad (3)$$

The tree-level $g \rightarrow q\bar{q}$ and $g \rightarrow gg$ collinear splitting functions are obtained by projecting the $\mathcal{O}(\alpha_s)$ expression for the discontinuity of the gluon propagator onto the physical degrees of freedom of the gluon field, using the polarization sum in a physical gauge [94]. Gauge invariance of the underlying Born matrix element and the relation $k_t^2 = -2p_i p_j z_i z_j$, derived from Eq. (2), result in the familiar expressions

$$P_{gq}^{\mu\nu}(p_i, p_j, \bar{n}) = T_R \left[-g^{\mu\nu} + 4z_i z_j \frac{k_t^\mu k_t^\nu}{k_t^2} \right], \quad (4)$$

$$P_{gg}^{\mu\nu}(p_i, p_j, \bar{n}) = C_A \left[-g^{\mu\nu} \left(\frac{z_i}{z_j} + \frac{z_j}{z_i} \right) - 2(1 - \varepsilon) z_i z_j \frac{k_t^\mu k_t^\nu}{k_t^2} \right].$$

The spin-averaged quark splitting function in the collinear limit can be obtained by projecting the vertex function onto the collinear direction [94], leading to

$$P_{qq}(p_i, p_j, \bar{n}) = C_F \left[\frac{2z_i}{z_j} + (1 - \varepsilon)(1 - z_i) \right]. \quad (5)$$

We define the difference of the full splitting functions of Eqs. (4) and (5) and their eikonal limit as the *purely collinear* splitting function, $P_{\parallel}(p_i, p_j)$. Using the known spin dependence of the quark splitting function, we obtain the following spin-dependent and spin-averaged expressions for final-state splittings (denoted by a superscript (F))

$$\begin{aligned} P_{qq\parallel}^{ss'}(F)(p_i, p_j, \bar{n}) &= \delta^{ss'} C_F (1 - \varepsilon)(1 - z_i), & P_{qq\parallel}^{(F)}(p_i, p_j, \bar{n}) &= C_F (1 - \varepsilon)(1 - z_i), \\ P_{gg\parallel}^{\mu\nu}(F)(p_i, p_j, \bar{n}) &= -2C_A (1 - \varepsilon) z_i z_j \frac{k_t^\mu k_t^\nu}{k_t^2}, & P_{gg\parallel}^{(F)}(p_i, p_j, \bar{n}) &= 2C_A z_i z_j, \\ P_{gq\parallel}^{\mu\nu}(F)(p_i, p_j, \bar{n}) &= P_{gq\parallel}^{\mu\nu}(p_i, p_j), & P_{gq\parallel}^{(F)}(p_i, p_j, \bar{n}) &= T_R \left[1 - \frac{2z_i z_j}{1 - \varepsilon} \right]. \end{aligned} \quad (6)$$

At this point we would like to stress that z_i and z_j depend on the precise form of the momentum mapping, and that they are not necessarily identical to the parton-shower splitting variables z and $1 - z$. This has implications in particular for the splitting functions in initial-state evolution and will be discussed in Secs. III A and III B.

Crossing parton i into the initial state, we obtain the following collinear factorization formula

$$n\langle 1, \dots, n | 1, \dots, n \rangle_n = \sum_{\lambda, \lambda' = \pm} n_{-1} \langle 1, \dots, \check{\lambda}(ij), \dots, \check{\lambda}', \dots, n | \frac{8\pi\alpha_s P_{(ij)i}^{\lambda\lambda'}(x)}{2p_i p_j x} | 1, \dots, \check{\lambda}(ij), \dots, \check{\lambda}', \dots, n \rangle_{n-1}, \quad (7)$$

where $x = 1/z$ is the momentum fraction of parton (ij) with respect to the initial-state parton i . Equation (1) is obtained from Eq. (1) via the crossing relation $P_{ab}(1/x) = -P_{ab}(x)/x$ [85, 95]. The splitting functions $P_{ab}^{\lambda\lambda'}(x)$ are therefore determined by Eqs. (4) and (5). However, the matching to the soft radiation pattern differs for initial-state splittings, because an initial-state particle of vanishing energy will lead to a vanishing cross section (see for example Sec.5.4 in [96]). This leads to the following expressions for the flavor-diagonal splitting functions in the initial state (denoted by a superscript (I))

$$P_{qq\parallel}^{(I)}(p_i, p_j, \bar{n}) = P_{qq}(p_i, p_j, \bar{n}), \quad P_{gg\parallel}^{(I)}(p_i, p_j, \bar{n}) = C_A \left[-g^{\mu\nu} x_i x_j + 2(1 - \varepsilon) \frac{x_j k_t^\mu k_t^\nu}{x_i k_t^2} \right]. \quad (8)$$

All other purely collinear splitting functions remain the same. We have simplified the notation by defining $x_i = 1/z_i$ and $x_j = -x_i z_j$. We stress again that differences in the purely collinear components of the spin-averaged DGLAP splitting functions can arise from the fact that x_i may not be equal to x , where x is the initial-state parton shower splitting variable. In practical applications, this typically leads to a suppression of $1/x$ enhanced parton splittings at large transverse momenta. We will return to this question in Secs. III A and III B, see in particular the discussion following Eq. (20).

B. Soft limit and soft-collinear matching

In the limit that gluon j becomes soft, the squared amplitude factorizes as [83]

$$n\langle 1, \dots, n | 1, \dots, n \rangle_n = -8\pi\alpha_s \sum_{i, k \neq i, j} n_{-1} \langle 1, \dots, \check{\lambda}, \dots, n | \mathbf{T}_i \mathbf{T}_k w_{ik,j} | 1, \dots, \check{\lambda}, \dots, n \rangle_{n-1}, \quad (9)$$

where \mathbf{T}_i and \mathbf{T}_k are the color insertion operators defined in [83, 96]. In the ALARIC parton-shower algorithm [63], the eikonal factor $w_{ik,j}$ is split into an angular radiator $W_{ik,j}$ and the gluon energy according to $w_{ik,j} = W_{ik,j}/E_j^2$. The angular radiator function

$$W_{ik,j} = \frac{1 - \cos \theta_{ik}}{(1 - \cos \theta_{ij})(1 - \cos \theta_{jk})} \quad (10)$$

is matched to the collinear splitting functions by partial fractioning:

$$W_{ik,j} = \bar{W}_{ik,j}^i + \bar{W}_{ki,j}^k, \quad \text{where} \quad \bar{W}_{ik,j}^i = \frac{1 - \cos \theta_{jk}}{2 - \cos \theta_{ij} - \cos \theta_{jk}} W_{ik,j}. \quad (11)$$

In the collinear limit for partons i and j , the eikonal factor $w_{ik,j}$ can be identified with the eikonal term of the DGLAP splitting functions $P_{aa}(z)$. Matching the soft to the collinear splitting functions in the improved large- N_c limit is achieved by replacing

$$\frac{P_{(ij)i}^{(F)}(p_i, p_j, \bar{n})}{2p_i p_j} \rightarrow \frac{\mathbf{T}_{ij}^2}{N_{\text{spec}}} \sum_{k \in \text{spec}}^{N_{\text{spec}}} \left[\delta_{(ij)i} \frac{\bar{W}_{ik,j}^i}{E_j^2} + \delta_{(ij)j} \frac{\bar{W}_{jk,i}^j}{E_i^2} \right] + \frac{P_{(ij)i\parallel}^{(F)}(p_i, p_j, \bar{n})}{2p_i p_j}, \quad (12)$$

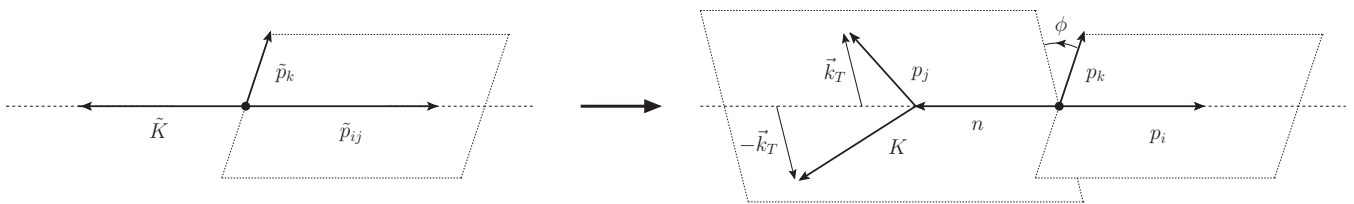


FIG. 1. Sketch of the momentum mapping for soft radiation and initial-state splittings. All momenta are considered outgoing. Note that p_k only acts as a reference for the definition of the azimuthal angle ϕ . See the main text for details.

where the sum runs over all color-connected partons, and N_{spec} stands for the number of color spectators. While initial-state parton evolution must respect Gribov-Lipatov reciprocity [85, 95], we need to take into account that the amplitude cannot develop a soft singularity in the initial-state momentum. Therefore,

$$\frac{P_{i(ij)}^{(I)}(p_i, p_j, \bar{n})}{2p_i p_j x} \rightarrow \delta_{i(ij)} \frac{\mathbf{T}_{ij}^2}{N_{\text{spec}}} \sum_{k \in \text{specs}}^{N_{\text{spec}}} \frac{\bar{W}_{ik,j}^i}{E_j^2} + \frac{P_{i(ij)\parallel}^{(I)}(p_i, p_j, \bar{n})}{2p_i p_j x}. \quad (13)$$

The two soft contributions to the gluon splitting function are treated as two different radiators [54]. The soft matching introduces a dependence of the splitting functions on the color spectators, k , and their momenta define directions independent of \hat{p}_{ij} [63].

III. MOMENTUM MAPPING

Parton shower algorithms are based on the notion of adding additional partons to an already existing ensemble of particles, while maintaining four-momentum conservation and on-shell conditions. This procedure requires a method to map the momenta of the Born process to a kinematical configuration after emission. The mappings are linked to the factorization of the differential phase-space element for a multi-parton configuration. Collinear safety a basic requirement for their construction. In addition, a mapping is NLL-safe if it preserves the topological features of previous radiation [56, 57]. Since the momentum mapping in most modern parton showers has been identified as the main stumbling block to achieving next-to-leading logarithmic precision, we will begin the description of ALARIC's initial-state evolution algorithm by discussing the kinematics.

A. Soft radiation kinematics

This section details the algorithm for the construction of momenta in soft emissions. The momentum mapping is sketched in Fig. 1. We identify the splitter momentum, \tilde{p}_i , and define a recoil momentum, \tilde{K} . In contrast to conventional dipole-like parton showers where the recoil momentum is usually given by the color spectator, in ALARIC this momentum can be chosen freely, with the condition that it must provide a hard scale. In most practical applications we will define \tilde{K} as the sum of all final-state momenta (in the case of final-state branchings also including the momentum of the splitting particle). Together, the momenta \tilde{K} and \tilde{p}_i define the reference frame of the splitting. The momentum of the color spectator, \tilde{p}_k , defines an additional direction, and provides the reference for the azimuthal angle, ϕ . To obtain the momenta after emission, the emitter is scaled by a factor z , and the emitted momentum, p_j , is constructed with transverse momentum component \vec{k}_T and suitable light-cone momenta. The recoil is absorbed by all particles that constitute the recoil momentum \tilde{K} . To parametrize the splitting kinematics, we make use of some of the notation in [63, 96], in particular

$$v = \frac{p_i p_j}{\tilde{p}_i \tilde{K}} \quad \text{and} \quad z = \frac{p_i \tilde{K}}{\tilde{p}_i \tilde{K}}. \quad (14)$$

The momentum mapping for emitter \tilde{p}_i and recoil momentum \tilde{K} is fixed by

$$\begin{aligned} p_i &= z \tilde{p}_i, \\ p_j &= (1-z) \tilde{p}_i + v(\tilde{K} - (1-z+2\kappa) \tilde{p}_i) - k_\perp, \\ K &= \tilde{K} - v(\tilde{K} - (1-z+2\kappa) \tilde{p}_i) + k_\perp, \end{aligned} \quad (15)$$

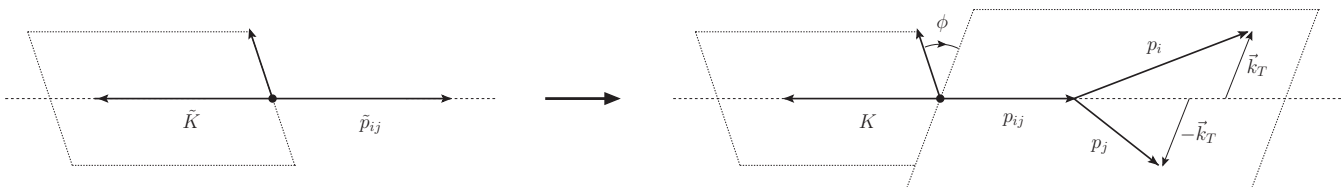


FIG. 2. Sketch of the momentum mapping for collinear radiation. All momenta are considered outgoing. Note that, again, p_k only acts as a reference for the definition of the azimuthal angle ϕ . See the main text for details.

with the absolute value of the transverse momentum given by

$$k_{\perp}^2 = v(1-v)(1-z)2\tilde{p}_i\tilde{K} - v^2\tilde{K}^2. \quad (16)$$

For initial-state splitters, the energy fraction z is replaced by $1/x$. If the momentum \tilde{K} is composed of the two initial-state momenta, all final-state momenta are subjected to a Lorentz transformation

$$p_l^{\mu} \rightarrow \Lambda_{\nu}^{\mu}(K, \tilde{K}) p_l^{\nu}, \quad \text{where} \quad \Lambda_{\nu}^{\mu}(\tilde{K}, K) = g_{\nu}^{\mu} - \frac{2(K + \tilde{K})^{\mu}(K + \tilde{K})_{\nu}}{(K + \tilde{K})^2} + \frac{2K^{\mu}\tilde{K}_{\nu}}{\tilde{K}^2}. \quad (17)$$

If the momentum \tilde{K} is composed of final-state momenta, those momenta are subjected to a Lorentz transformation $p_l^{\mu} \rightarrow \Lambda_{\nu}^{\mu}(\tilde{K}, K) p_l^{\nu}$, with $\Lambda_{\nu}^{\mu}(\tilde{K}, K)$ given by Eq. (17).

It remains to determine the variables z_i and z_j in Sec. II, which are needed to evaluate the purely collinear splitting functions. Expanding Eq. (15) in terms of the large forward light-cone momentum, $\hat{p}_{ij}^{\mu} = p_{ij}^{\mu} - p_{ij}^2/(2p_{ij}\bar{n})\bar{n}^{\mu}$, the small transverse components, and the very small anti-collinear components, we obtain

$$p_i = \frac{z}{1-v(1-z+\kappa)}\hat{p}_{ij} + \frac{z}{1-v(1-z+\kappa)}k_{\perp} + \mathcal{O}\left(\frac{k_{\perp}^2}{2\tilde{p}_i\tilde{K}}\right), \quad (18)$$

$$p_j = \frac{(1-z)(1-v)-v\kappa}{1-v(1-z+\kappa)}\hat{p}_{ij} - \frac{z}{1-v(1-z+\kappa)}k_{\perp} + \mathcal{O}\left(\frac{k_{\perp}^2}{2\tilde{p}_i\tilde{K}}\right).$$

Having obtained an expression equivalent to Eq. (2), it is apparent that the momentum fractions that appear in the purely collinear splitting functions, Eqs. (6) and (8) are given by

$$z_i = \frac{z}{1-v(1-z+\kappa)}, \quad z_j = 1 - \frac{z}{1-v(1-z+\kappa)}. \quad (19)$$

In initial-state evolution, the replacements $z \rightarrow 1/x$, $z_i \rightarrow 1/x_i$ and $z_j \rightarrow -x_j/x_i$ change Eq. (19) to

$$x_i = x + v - vx(1+\kappa), \quad x_j = 1 - x - v + vx(1+\kappa). \quad (20)$$

In addition, the transverse momentum k_{\perp}^{μ} appearing in the Sudakov decomposition Eq. (2), and hence in the spin-dependent splitting functions in Sec. II, is expressed in terms of the radiation kinematics variables appearing in Eq. (15) as $z_i k_{\perp}^{\mu}$ [96]. Note that for initial-state emissions with the spectator being the complete final state, Eq. (20) simplifies to $x_i = x + v$ and $x_j = 1 - x - v$. This relation has been used in the context of a Catani-Seymour dipole shower in Refs. [81, 82] to obtain an improved approximation of the splitting functions and generally leads to a reduction of emission probabilities from terms in the splitting functions that are proportional to $1/x_i$.

B. Collinear splitting kinematics

As discussed in Sec. (II), collinear parton evolution is easier understood in a phase-space parametrization where the splitting products compensate each others transverse recoil with respect to the direction of the progenitor. For the implementation of the purely collinear components of final-state splitting functions we therefore choose a kinematics mapping that is closely related to [60, 76]. It has been shown [60] that this type of mapping satisfies the criteria for NLL precision if it is applied to the purely collinear splitting functions only. The proof rests on similar arguments as the proof of accuracy for the radiation kinematics of Sec. III A [63].

The momentum mapping is sketched in Fig. 2. We identify the splitter momentum, \tilde{p}_i , and define a longitudinal recoil momentum, \tilde{K} . Again, this recoil momentum can be freely defined. In most practical applications we use the sum of final-state momenta, excluding the momentum of the splitter. Together, the momenta \tilde{K} and \tilde{p}_i define the reference frame of the splitting. And, as before, the momentum of the color spectator, \tilde{p}_k , defines an additional direction, which provides the reference for the azimuthal angle, ϕ . To obtain the momenta after emission, we invoke the massive splitting kinematics of [89], in which the emitter is scaled and the momentum K absorbs the longitudinal recoil, while the transverse recoil is compensated locally between the splitting products. We make use of some of the notation in [96], in particular

$$y = \frac{p_i p_j}{p_i p_j + (p_i + p_j) \tilde{K}} \quad \text{and} \quad z = \frac{p_i \tilde{K}}{(p_i + p_j) \tilde{K}}, \quad (21)$$

and we define $\kappa = K^2 / (2\tilde{p}_{ij} \tilde{K})$. In terms of the additional variables

$$\zeta = \frac{1 + y - \sqrt{(1-y)^2 - 4y\kappa}}{2y(1+\kappa)}, \quad \bar{z} = \frac{z(1-y)\zeta(1-\zeta y) - \zeta^2 y \kappa}{(1-\zeta y)^2 - \zeta^2 y \kappa}, \quad (22)$$

the momenta after the splitting are given by

$$\begin{aligned} p_i^\mu &= \bar{z} \frac{\tilde{p}_{ij}^\mu}{\zeta} + (1 - \bar{z}) y \zeta (\tilde{K}^\mu - \kappa \tilde{p}_{ij}^\mu) + k_\perp^\mu, \\ p_j^\mu &= (1 - \bar{z}) \frac{\tilde{p}_{ij}^\mu}{\zeta} + \bar{z} y \zeta (\tilde{K}^\mu - \kappa \tilde{p}_{ij}^\mu) - k_\perp^\mu, \\ K^\mu &= \left(1 - \frac{1 - y \kappa \zeta^2}{\zeta}\right) \tilde{p}_{ij}^\mu + (1 - y \zeta) \tilde{K}^\mu. \end{aligned} \quad (23)$$

The transverse momentum squared is given by

$$k_\perp^2 = y \bar{z} (1 - \bar{z}) 2\tilde{p}_{ij} \tilde{K}. \quad (24)$$

This particular scheme cannot be used in initial-state splittings, because the momentum of the splitter and at least one of the splitting products must be aligned. We therefore use the soft radiation kinematics also for the purely collinear initial-state splittings. If the momentum \tilde{K} was constructed from multiple final-state momenta, those momenta are subjected to a Lorentz transformation $p_l^\mu \rightarrow \Lambda_\nu^\mu(\tilde{K}, K) p_l^\nu$, with $\Lambda_\nu^\mu(\tilde{K}, K)$ given by Eq. (17).

Equation (23) has the form of Eq. (2), and we can read off the momentum fractions that appear in the purely collinear splitting functions, Eqs. (6) and (8):

$$z_i = \bar{z} \quad \text{and} \quad z_j = 1 - \bar{z} \quad (25)$$

with the transverse momentum squared, k_i^2 , in collinear splitting kinematics given by Eq. (24). Note that this relation differs from the definition $z_i = z$ in a Catani-Seymour dipole like final state parton shower only due to the mass of the recoil momentum. In particular, it is identical if $\kappa = 0$, as for example in the first emission in $e^+e^- \rightarrow \text{hadrons}$, or in pure jet production at hadron colliders.

IV. THE EVOLUTION ALGORITHM

For initial-state evolution, we use the original definition of the evolution variable in [63]. It is related to the energies and polar angle in the rest frame of n , where we have the simple relations

$$E_i = z \frac{\tilde{p}_i \tilde{K}}{\sqrt{n^2}}, \quad E_j = E_i \frac{1-z}{z}, \quad \text{and} \quad n^2 = 2\tilde{p}_i \tilde{K} (1-z + \kappa). \quad (26)$$

The polar angle, θ_j , of the emission is given by

$$1 - \cos \theta_j^i = 2v \frac{1-z + \kappa}{1-z}. \quad (27)$$

In terms of these quantities, the initial-state evolution variable is defined as (see Eq. (41) of [63])

$$t^{(n)} = 2E_j^2 (1 - \cos \theta_j^i) = v(1-z) 2\tilde{p}_i \tilde{K}. \quad (28)$$

The same definition can also be used for final-state evolution. However, we also introduce a variant of the original proposal, which will become our default choice: We determine the evolution variable using energies and angles in the rest frame of the recoil momentum, K , after the emission. In the soft limit, $p_j \rightarrow 0$, this frame coincides with the frame defined by n . The energies of particles i and j in the K -frame are given by

$$E_i = (1-v) \frac{z \tilde{p}_i \tilde{K}}{\sqrt{\tilde{K}^2}}, \quad E_j = \frac{E_i}{1-v} \frac{1-z}{z}. \quad (29)$$

The polar angle θ_j^i of the emission is determined by

$$1 - \cos \theta_j^i = \frac{2\kappa}{1-z} \frac{v}{1-v}. \quad (30)$$

The final-state evolution variable of the parton shower in this scheme is defined as

$$t^{(K)} = 2E_j^2 (1 - \cos \theta_j^i) = \frac{v}{1-v} (1-z) 2\tilde{p}_i \tilde{K}. \quad (31)$$

The advantage of the redefinition is a simplified determination of the upper bound on the evolution variable. For example, in color singlet decays one has $t^{(K)} \leq \sqrt{\tilde{K}^2}$. The Jacobian factor for the transformation $\ln v \rightarrow \ln t$ is given by $(1-z)/(1-z+\tau)$. We will investigate the numerical effect of different choices for the evolution scheme in Sec. VI.

V. MULTI-JET MERGING

The physics modeling of parton-shower simulations can be improved systematically with the help of multi-jet merging [21–31]. This is achieved by including higher multiplicity tree-level fixed order calculations with well separated parton-level jets, while maintaining both the logarithmic accuracy of the parton shower and the fixed order accuracy. Here, we implement the leading-order merging method described in [25], which can be described as follows:

1. The phase space of parton-shower emissions is restricted to the complement of the phase space of the fixed-order calculations. For example, in the combination of $pp \rightarrow Z$ and $pp \rightarrow Zj$, with $p_{T,j} \geq p_{T,\text{cut}}$, the phase space of the first parton-shower emission would be restricted to $p_\perp < p_{\perp,\text{cut}}$. This is called the jet veto, the variable used to separate the phase space is called the jet criterion, and the separation scale is called the merging scale, Q_{cut} .
2. The fixed-order result is modified to include higher-order corrections as resummed in the parton-shower approach. This procedure consists of multiple steps:
 - (a) Re-interpreting the final-state configuration of the fixed-order calculation as having originated from a parton cascade [97]. This is called *clustering*, and the representations of the final-state configuration in terms of parton branchings are called parton-shower histories.
 - (b) Choosing appropriate scales for evaluating the strong coupling at each branch point in the cascade, thereby resumming higher-order corrections to soft-gluon radiation [98, 99]. This procedure is called α_s -reweighting.
 - (c) Weighting by appropriate no-emission probabilities, representing the resummed unresolved real and virtual corrections [21]. This procedure is called Sudakov reweighting. It is implemented using pseudo showers [22].

The jet clustering procedure for the ALARIC parton shower requires extra care, because multiple histories (soft and collinear) may exist for each combination of external partons. Due to the difference between radiation and splitting kinematics, they differ not only in their associated weight, but also in the kinematics of the underlying Born state.

VI. NUMERICAL RESULTS

In this section we present first numerical results obtained with the ALARIC parton shower for hadron colliders, as implemented in the event generation framework SHERPA [100–102]. We set $C_F = (N_c^2 - 1)/(2N_c) = 4/3$ and $C_A = 3$, all quarks are considered as massless, but we implement flavor thresholds at $m_c = 1.42$ GeV and $m_b = 4.92$ GeV. The running coupling is evaluated at two loop accuracy with $\alpha_s(m_z) = 0.118$. Following standard practice to improve the logarithmic accuracy of the parton shower, we employ the CMW scheme [99], *i.e.* the soft eikonal contribution to the flavor conserving splitting functions is rescaled by $1 + \alpha_s(t)/(2\pi)K$, with $K = (67/18 - \pi^2/6)C_A - 10/9 T_R n_f$. Where appropriate, our results include multi-jet merging at leading-order accuracy. All analyses are performed with Rivet [103].

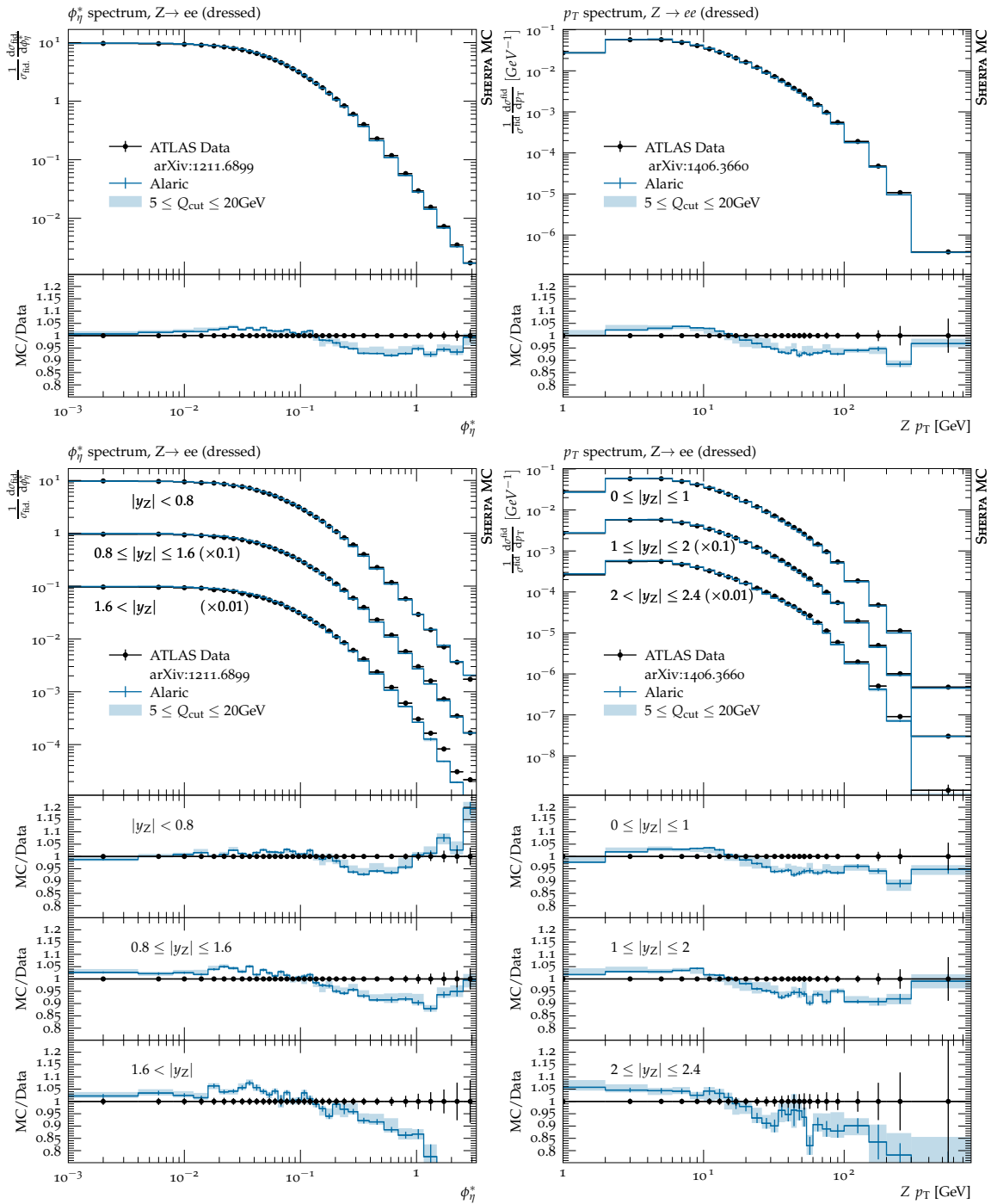


FIG. 3. ALARIC ME+PS merged predictions with up to three jets for ϕ_η^* (left) and the Z -boson p_T (right), inclusive over all accessible Z -boson rapidities (upper panel), or in different bins of $|y_z|$. Uncertainties related to the choice of merging cut Q_{cut} are indicated with the light-blue band around the central value; the main plots show the overall prediction in comparison to the ATLAS data at 7 TeV c.m.-energy from [104] and [105], while respective lower panels show deviations.

A. Drell-Yan lepton pair production

Figure 3 shows the transverse momentum spectrum of the Drell-Yan lepton pair, and the angular variable ϕ_η^* [106], as predicted by a multi-jet merged calculation with ALARIC, in comparison to experimental data from the ATLAS collaboration [104, 105]. In this analysis, leptons are required to have $|\eta| < 2.4$ and $p_T > 20$ GeV, in addition to the invariant mass constraint $66 \text{ GeV} \leq m_{ll} \leq 116 \text{ GeV}$. The leptons are dressed, *i.e.*, they are combined with photons

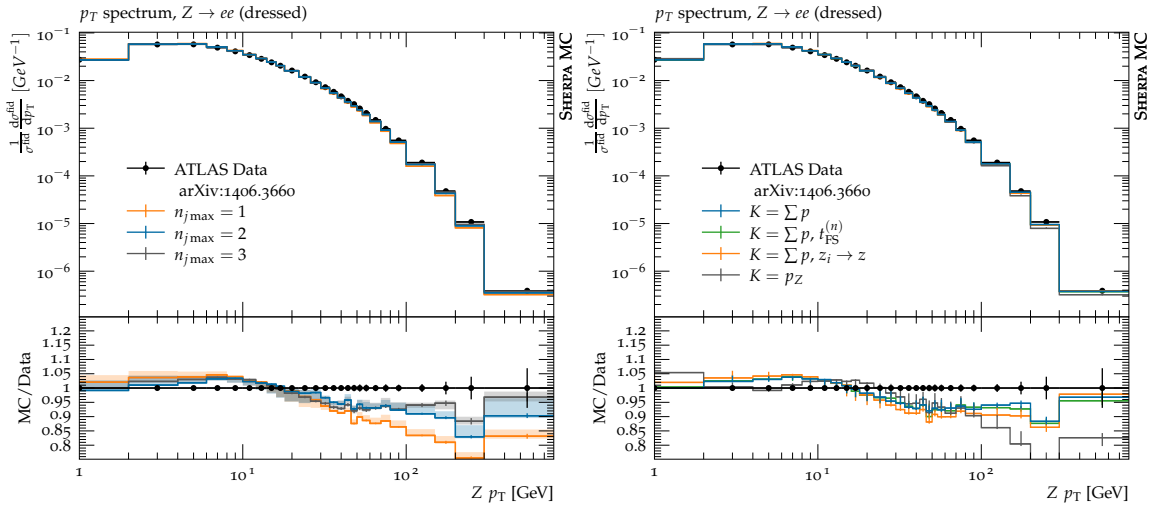


FIG. 4. Systematic uncertainties of parton-shower predictions from ALARIC due to different maximal number, $n_{j,\max}$ of jet from leading-order matrix elements (left) and due to different choices of the recoil momentum \vec{K} (right). See Fig. 3 and the main text for details.

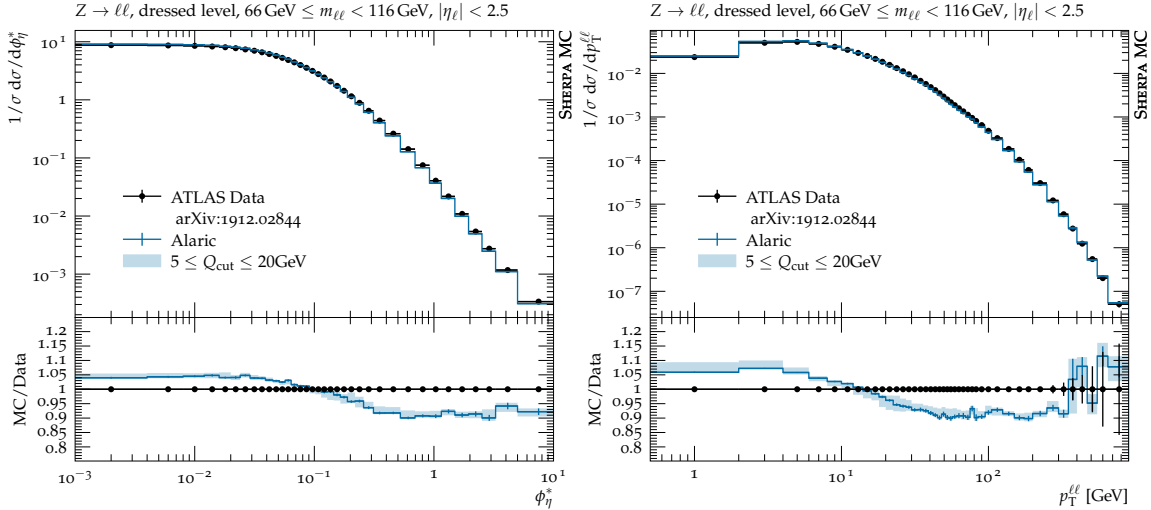


FIG. 5. ALARIC ME+PS merged predictions in comparison to ATLAS data from [107].

within a cone of radius $R = 0.1$. The uncertainty band in Fig. 3 corresponds to the variation of the merging cut between 5 GeV and 20 GeV. In general, we find agreement with experimental data to the level that it can be expected from a parton-shower simulation without NLO multi-jet merging, see for example [28]. Apart from very forward regions in Z -boson rapidity, the deviations from data reach at most five to ten percent.

We include up to three jets in this simulation, but we note that the prediction stabilizes upon including the second jet, *cf.* the left panel of Fig. 4. There, we display a variation of results with the highest jet multiplicity, $n_{j,\max}$, the maximal number of jets described by fixed-order calculations in the multi-jet merging. We find that with increasing $n_{j,\max}$ the high transverse momentum region is better described by the simulation. This effect has been discussed in great detail in the original literature on multi-jet merging [21–24]. The saturation of this effect at $n_{j,\max} = 2$ can be understood by noticing that the addition of a first and second jet adds new partonic initial state channels.

The right panel of Fig. 4 shows some of the systematic uncertainties associated with the parton-shower prediction itself. We compare two different definitions of K , one where the recoil is absorbed by the Drell-Yan lepton pair (labeled $K = p_z$), and one where the recoil is absorbed by the complete final state (our default choice, labeled $K = \sum p$). While the first definition leads to a somewhat better description of the transverse momentum spectrum in the bulk of the distribution, it fails in the high- p_T tails. This is expected, because in the high transverse momentum region, the invariant mass of the Drell-Yan lepton pair no longer provides the highest scale in the process. We also compare

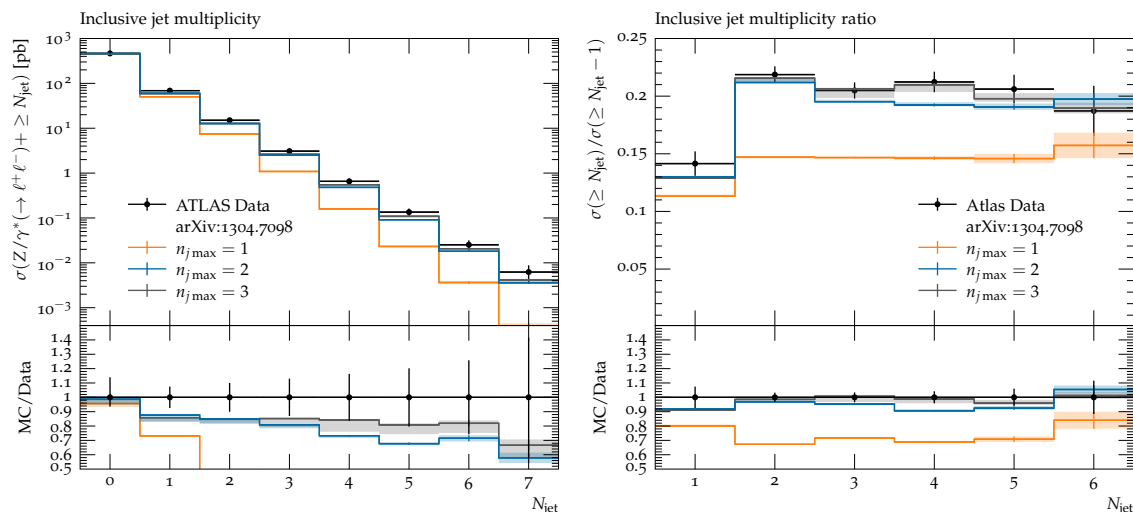


FIG. 6. Multi-jet merged predictions from ALARIC in comparison to ATLAS measurements at 7 TeV [108], again in dependence on $n_{j \max}$. See the main text for details.

to a simulation where the momentum fractions z_i defined in Eq. (2) are replaced by the splitting variable z (labeled $K = \sum p$, $z_i \rightarrow z$). The differences compared to the default simulation are small, because the observable is largely insensitive to $1/x$ enhanced terms in the parton-shower splitting functions. Finally, we compare to a simulation where the new evolution scheme, described in Sec. IV, is replaced by the original proposal in [63] (labeled $K = \sum p$, $t_{\text{FS}}^{(n)}$). Again, the differences between the two options are small.

Figure 5 displays predictions from ALARIC in comparison to experimental data at 13 TeV c.m.-energy from the ATLAS collaboration reported in [107]. In this analysis, leptons are required to satisfy slightly different cuts, *i.e.* $|\eta| < 2.5$ and $p_T > 27$ GeV, in addition to the invariant mass constraint $66 \text{ GeV} \leq m_{ll} \leq 116 \text{ GeV}$. As before, the leptons have been dressed with a cone of radius $R = 0.1$. By far and large we observe similar features as in the comparison to 7 TeV data in the upper panel of Fig. 4.

Figure 6 displays jet-multiplicity spectra in Z + jets multi-jet merged predictions from ALARIC in comparison to measurements from the ATLAS collaboration [108]. There, electrons are required to have $|\eta| < 1.37$ or $1.52 < |\eta| < 2.47$ and muons must be within $|\eta| < 2.4$. Both electrons and muons must have $p_T > 20$ GeV and are required to satisfy the invariant mass constraint $66 \text{ GeV} \leq m_{ll} \leq 116 \text{ GeV}$. The leptons are dressed by photons within a cone of radius $R = 0.1$ and must satisfy $\Delta R_{ll} > 0.2$. Jets are reconstructed using the anti- k_T algorithm [110] with a radius of $R = 0.4$ and are required to have $|\eta| < 4.4$ and $p_T > 30$ GeV. In addition, they must be separated from leptons by $\Delta R > 0.5$. The left panel shows the inclusive jet multiplicity distribution, and the right panel displays the ratio of consecutive jet rates. We present Monte-Carlo results with increasing number of $n_{j \max}$ to exemplify that the correct modeling of these distributions depends on the appropriate coverage of the multi-jet phase space and the incorporation of the tree-level matrix elements at sufficiently high final-state multiplicity. A computation with $n_{j \max} = 1$ fails to describe the experimental data, while the calculations with $n_{j \max} = 2$ and $n_{j \max} = 3$ are fairly similar. In particular, the result with $n_{j \max} = 3$ is in good agreement with the jet multiplicity ratio measurement above $N_{\text{jet}} = 1$. The uncertainty bands shown in the figure represent the envelope of the statistical uncertainties and the merging cut variations, with the merging cut varied between 5 GeV and 20 GeV. We attribute the rate mismatch in the jet multiplicity distribution above $N_{\text{jet}} = 0$ and the corresponding mismatch at $N_{\text{jet}} = 1$ in the jet rate ratio to the missing higher-order corrections, which are larger for the one-jet rate and the subsequent jet rates than for the inclusive process [28, 111].

Figure 7 shows predictions from a Z +jets multi-jet merged computation with $n_{j \max} = 2$ in comparison with experimental measurements at 7 TeV c.m.-energy from CMS [109]. The upper left panel shows the transverse thrust distribution [112], and the upper right panel displays the same in the boosted region, where $p_{T,Z} > 150$ GeV. The lower left panel shows the azimuthal decorrelation between the Drell-Yan lepton pair and the leading jet, $\Delta\phi(Z, J1)$, and the lower right panel shows the same in the boosted region, where $p_{T,Z} > 150$ GeV. The Monte-Carlo predictions have been obtained with the same settings as in Fig. 4. The difference between the individual results is small, except for the azimuthal decorrelation in the boosted regime, where the recoil definition using only the di-lepton pair fails to describe the small- $\Delta\phi$ region. This is expected, because in the boosted regime the Drell-Yan invariant mass does not provide the largest scale in the process.

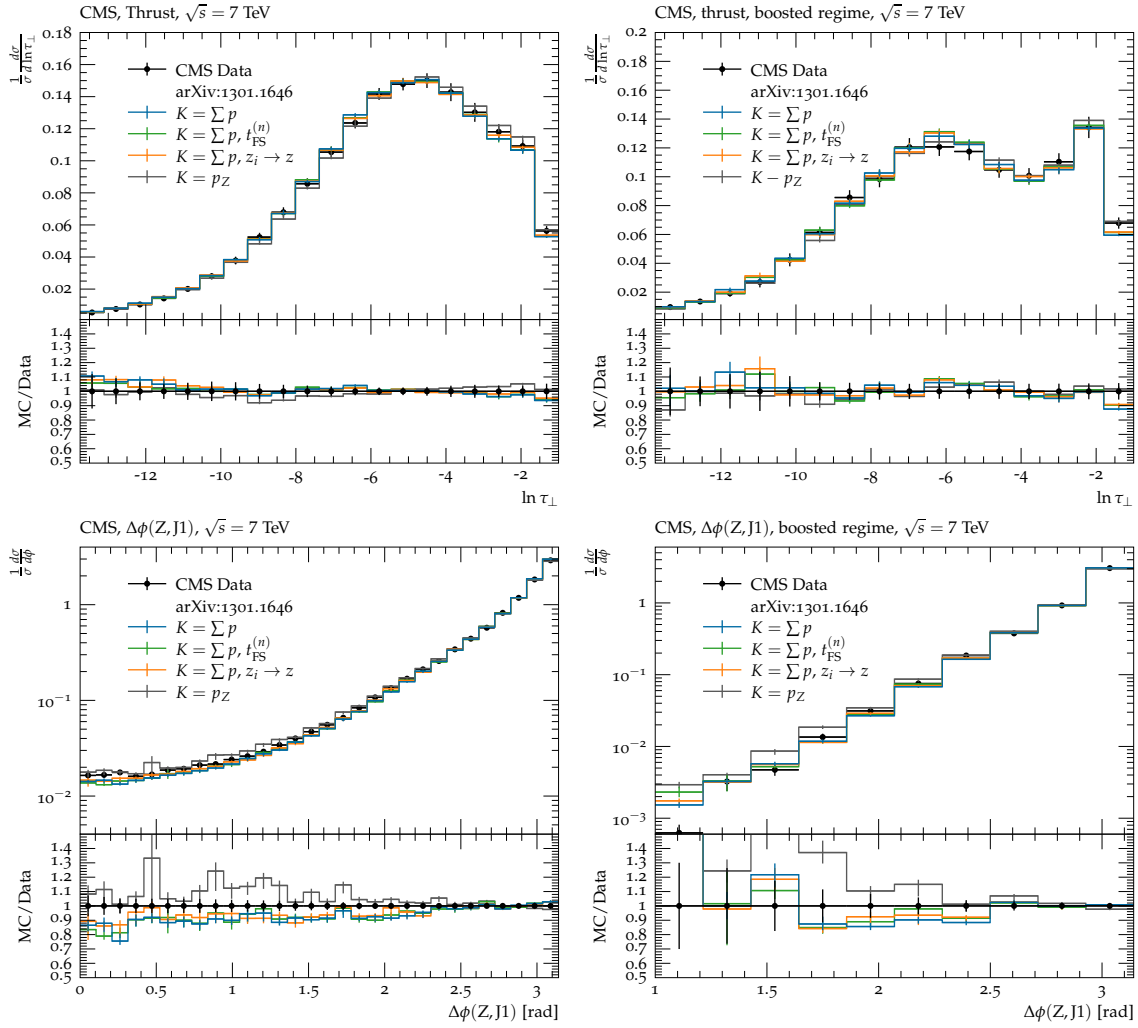


FIG. 7. Multi-jet merged predictions from ALARIC in comparison to CMS measurements [109]. See the main text for details.

B. Inclusive jet and di-jet production

In this sub-section we compare results from a pure parton-shower simulation, *without* applying any multi-jet merging, with ALARIC against inclusive jet and dijet measurements from the ATLAS and CMS collaborations. The renormalization and factorization scales are chosen as $\mu_R = \mu_F = H_T/4$, where H_T denotes the scalar sum of the final state transverse momenta. The resummation scale (*i.e.* the parton shower starting scale) is defined as $\mu_Q = p_\perp$, with p_\perp the transverse momentum of the leading jet. We compare to data measured at the LHC at $\sqrt{s} = 7$ TeV and $\sqrt{s} = 13$ TeV. Hadronization corrections are included using the Lund model via an interface to Pythia 8 [114]. We use the string fragmentation parameters $a = 0.4$, $b = 0.36$ and $\sigma = 0.3$. To simulate the underlying event we rely SHERPA's default module [101], based on the Sjöstrand–Zijl multiple-parton interaction (MPI) model [115]. It is worth noting that so far we have not produced a dedicated tune of hadronization or underlying event parameters specifically for the ALARIC parton shower.

We start our discussion by firstly comparing, in Fig. 8, ALARIC results to inclusive jet rates in dependence on the transverse momentum of the leading jet, in several bins of the leading jet rapidity. The data were taken by the CMS collaboration at $\sqrt{s} = 13$ TeV [113] and reach energy scales up to $p_\perp \sim 2$ TeV and rapidity values of up to $|y| = 4.7$. Our predictions are in good agreement with data, which motivates us to investigate the details of the radiation pattern in more detail.

We continue by comparing to the inclusive rates of jets produced in the shower to data measured by ATLAS [116] at $\sqrt{s} = 7$ TeV. The analysis constructs anti- k_t jets with a radius parameter of $R = 0.4$, and requires at least one jet with a transverse momentum of $p_\perp > 80$ GeV, while additional jets are required to have $p_\perp > 60$ GeV. All jets

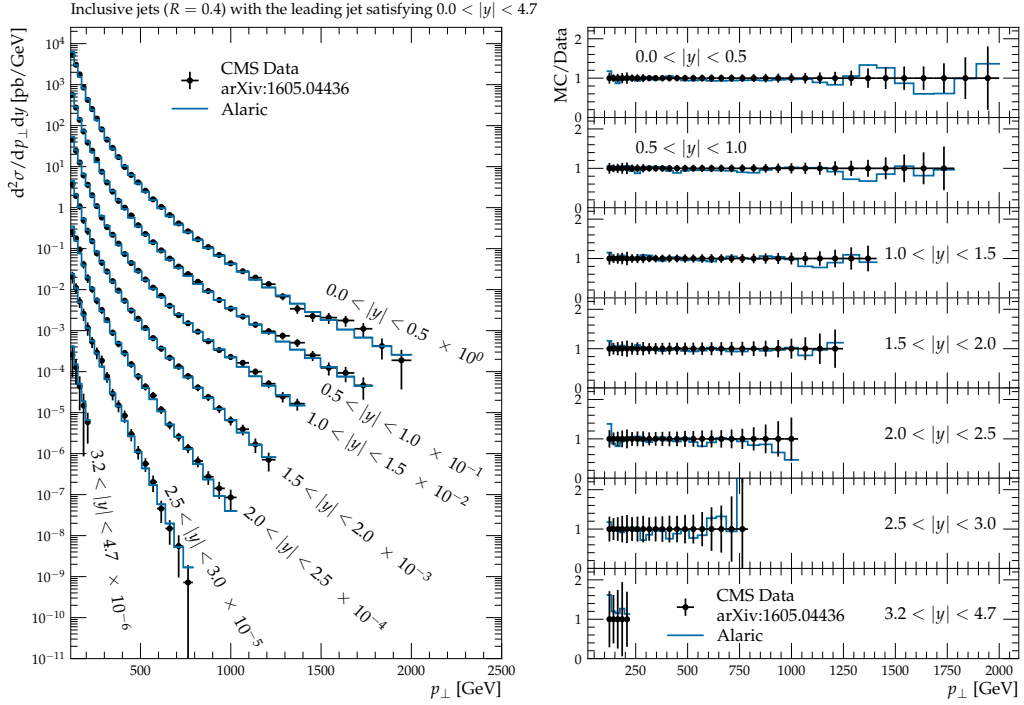


FIG. 8. Transverse momentum spectrum of inclusive jets in different rapidity regions in proton-proton collisions at a center of mass energy of 13 TeV. ALARIC predictions compared to data measured by CMS [113]. The left plot shows the full distributions while the panels on the right are the ratio to data.

must satisfy a rapidity requirement of $|y| < 2.8$. The comparison of the cross sections for inclusive jet is presented in Fig. 9, starting from $N_{\text{jet}} = 2$ and going up to $N_{\text{jet}} = 6$. The ALARIC predictions slightly overestimate the central value of the overall cross section for lower multiplicities and tend to drop off somewhat faster for higher jet rates than seen in data. However, the predictions are consistent with the data within the statistical uncertainties over the full range. The ratio plot in the middle of the upper left panel of Fig. 9 shows that the central value of the 3-jet rate (although within the data uncertainty) is overestimated slightly more than the inclusive 2-jet rate. This effect is echoed in the bottom of the upper left panel, where we plot the ratios of inclusive N_{jet} versus $N_{\text{jet}} - 1$ rate. In the upper right panel of Fig. 9 we compare to data for the ratio of the 3- to 2-jet rate, differential in the transverse momentum of the leading jet, with different minimal requirements on the hardness of the included jets. We can see that the relative enhancement is mostly constant over the full range of leading jet p_{\perp} . A similar dataset is available casting the 3-to-2-jet ratio as a function of the scalar sum of the transverse momenta of the two leading jets, $H_T^{(2)}$, or all jets, H_T . We compare with 7 TeV data from ATLAS [116], binned in $H_T^{(2)}$ in the lower left panel of Fig. 9, while the lower right plot compares the shower with a similar measurement by the CMS collaboration [117] binned in H_T . The CMS measurement, likewise performed at $\sqrt{s} = 7$ TeV, uses anti- k_t jets with an radius of $R = 0.5$ and requires a transverse momentum of at least $p_{\perp}^{\text{jets}} > 50$ GeV. The ALARIC predictions reproduce the data remarkably well, with practically no discrepancy to either ATLAS or CMS data within the uncertainty of the measurements. This emphasizes that the ALARIC algorithm can predict jet multiplicities and the 2-to-3 jet rate with excellent quality from the parton shower alone.

We now turn to more differential measurements of jet properties. The upper panel of Fig. 10 shows the transverse momentum spectra of the four leading jets (according to their p_{\perp}), as predicted by ALARIC, and compares the results to 7 TeV measurements from ATLAS [116], providing data for transverse momenta of the jets between 90 GeV and up to 800 GeV for the leading and sub-leading jet(s). The data are also available differential in the H_T observable, in the range $180 \text{ GeV} < H_T < 1600 \text{ GeV}$, separately for events containing at least 2, 3 and 4 jets. The comparison in the lower panel of Fig. 10 presents a similar picture as the transverse momentum data, the parton-shower result from ALARIC compares very well over the entire range and for all considered multiplicities. We again observe excellent agreement between our results and experimental data, independent of the jet selection and over the full range of transverse momentum studied.

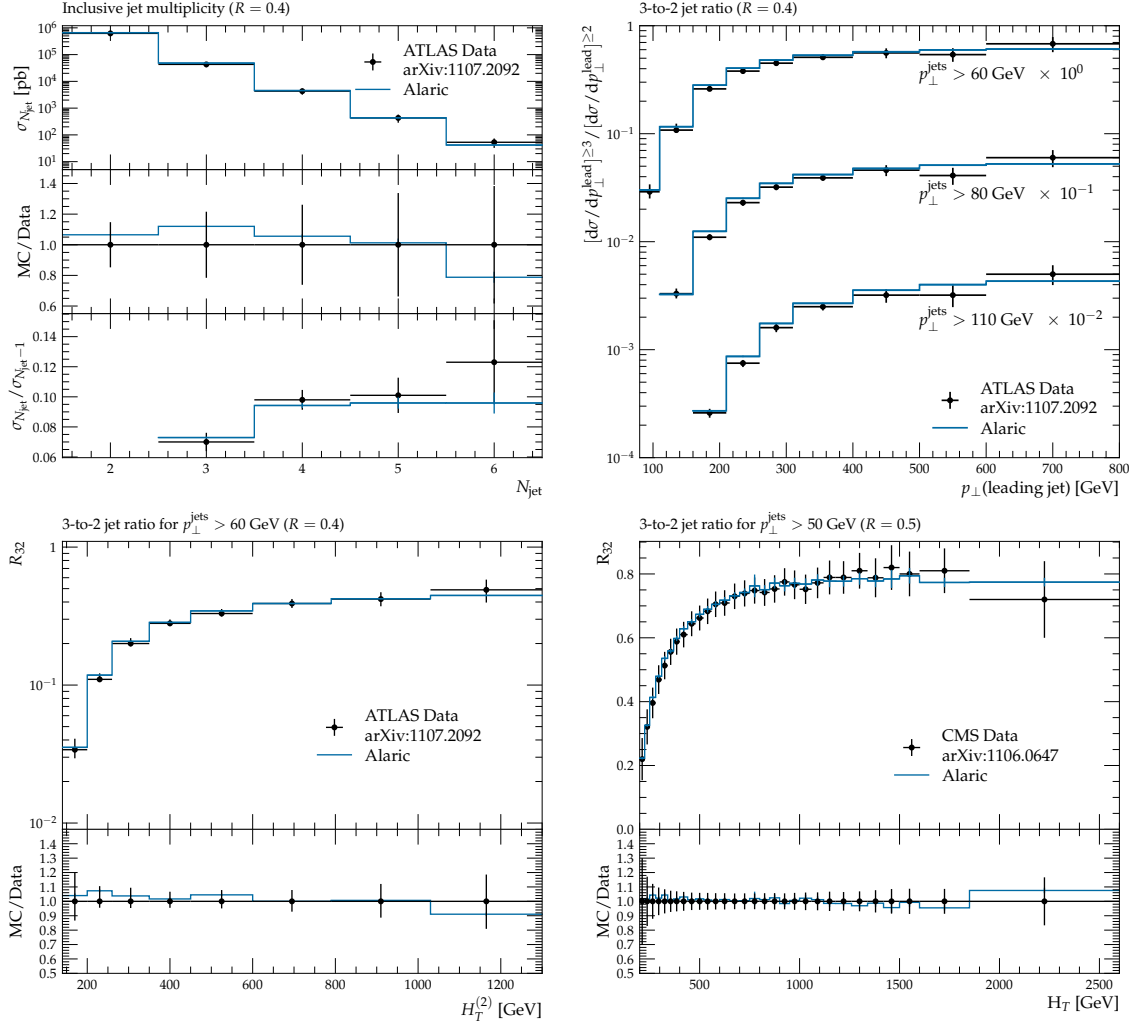


FIG. 9. Inclusive jet multiplicity in inclusive jet production at $\sqrt{s} = 7$ TeV (upper left panel) with cross sections (top), the ratio of simulation and data (middle) and ratios between $N_{\text{jet}} = 3$ to $N_{\text{jet}} = 2$ rates (right) differential in the transverse momentum of the leading jet (upper right panel); both sets of data are taken from [116]. Ratio of inclusive 3 jet over 2 jet rate R_{32} at $\sqrt{s} = 7$ TeV, as predicted by ALARIC and compared to measurements from ATLAS [116] (lower left) and CMS [117] (lower right).

While so far we have considered the transverse momenta and multiplicity distributions of leading jets in the events, we next analyze a class of observables sensitive to additional radiation in the event. To this end we consider non-global observables called gap fractions, *i.e.* the fraction of events with no jets harder than a cutoff Q_0 in the rapidity interval of size Δy between the two leading jets of a dijet system. We compare our results to data measured by the ATLAS experiment [118] at $\sqrt{s} = 7$ TeV in Fig. 11. This analysis uses anti- k_t jets with a radius of $R = 0.6$, and the measurement is presented in several Δy bins starting from $0 < \Delta y < 1$ ranging up to $7 < \Delta y < 8$. We observe excellent agreement of the data at larger Q_0 for the full range of Δy . Only for the smallest Q_0 values we find a slight excess of our parton-shower predictions over the data.

Finally, we highlight ALARIC's performance in describing the intra-jet dynamics by presenting a comparison to a jet substructure observable, in Fig. 12. The CMS collaboration has measured several variants of angularities [119] in dijet events at 13 TeV. This measurement has been studied extensively using Sherpa in the past [120, 121]. For brevity we restrict ourselves to showcasing the case of the so-called Les Houches angularity [122, 123] measured on charged particles in anti- k_t jets with radius $R = 0.8$. We observe a similar level of agreement to the data as these earlier studies, describing the general trend of the data but tentatively producing somewhat narrower distributions than seen in data.

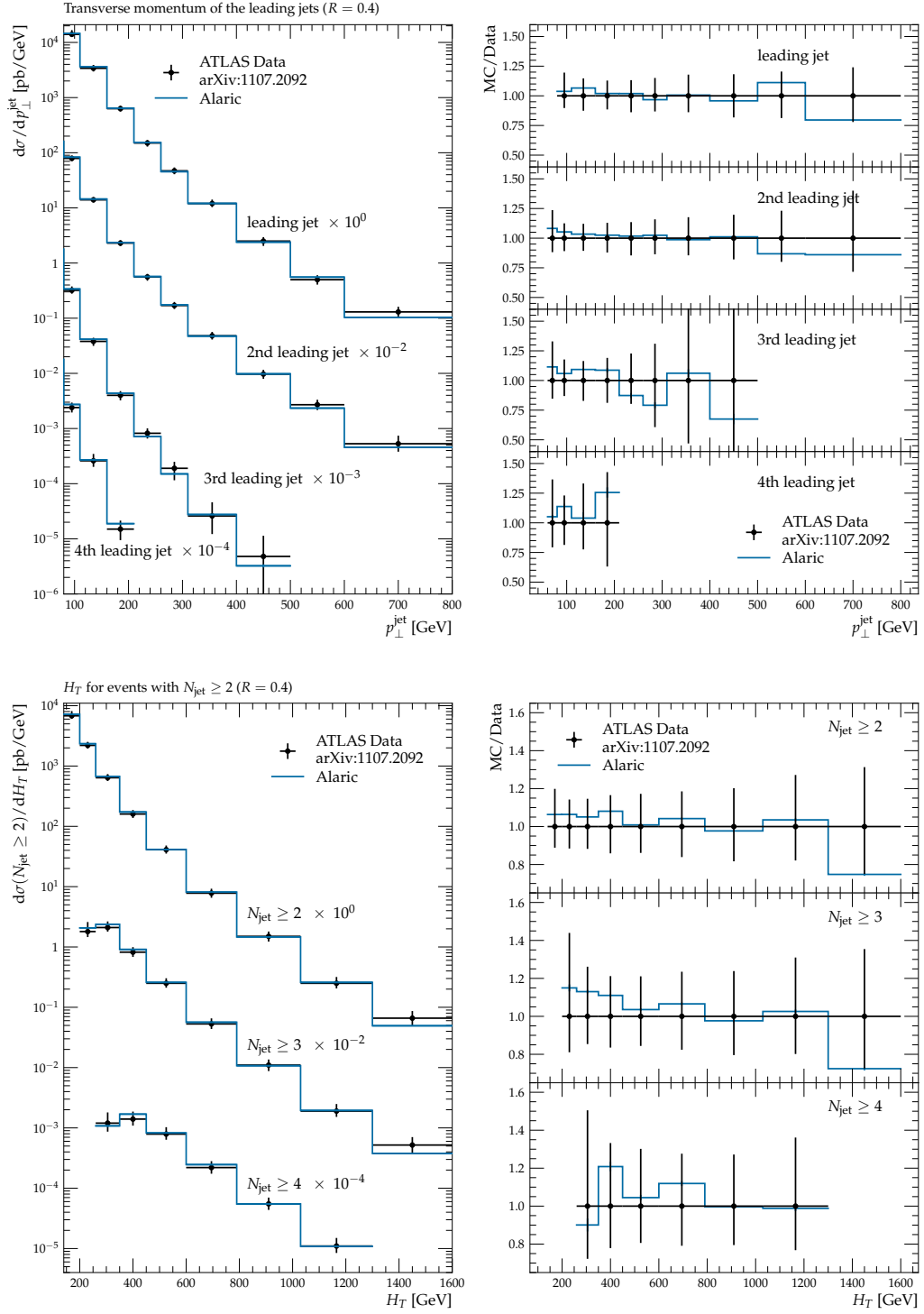


FIG. 10. Transverse momentum spectra for the first 4 leading jets as predicted by ALARIC (upper left) and the ratio of simulation and data (upper right). Cross sections differential in the H_T observable for events with at least 2, 3 and 4 hard jets (lower left) and the ratio of simulation and data (lower right), all with data from [116] taken at $\sqrt{s} = 7$ TeV.

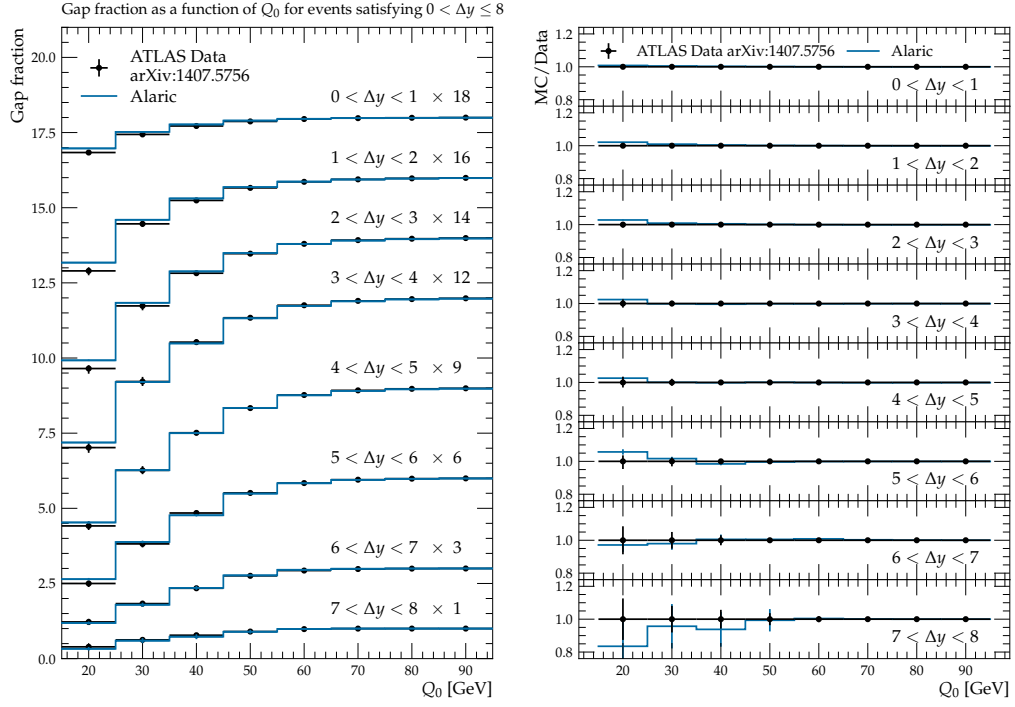


FIG. 11. Gap fractions as a function of the cutoff Q_0 for different rapidity gaps Δy . ALARIC predictions are compared to data measured by ATLAS [118] at $\sqrt{s} = 7$ GeV. The left plot shows the full distributions while the panels on the right are the ratio to data.

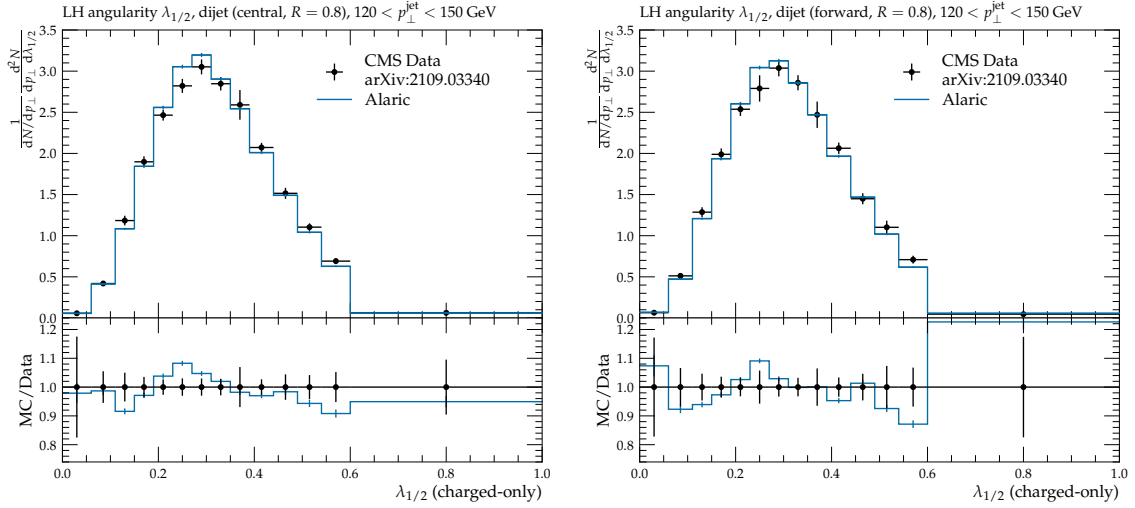


FIG. 12. Les Houches angularity as measured by CMS [119] at $\sqrt{s} = 13$ TeV, on the more central (left) and more forward (right) of the two leading jets in dijet events.

VII. CONCLUSIONS

In this publication we introduced the novel ALARIC parton-shower for simulating QCD radiation at hadron colliders, in particular the LHC. We emphasized the importance of a correct identification of the momentum fractions entering the purely collinear components of the splitting functions. We introduced a new evolution variable, which is defined in the frame of the recoil momentum after the emission. This frame coincides with the event frame in $e^+e^- \rightarrow$ hadrons. We also presented the first multi-jet merging for the ALARIC parton shower.

We quantified the systematic uncertainties of the parton-shower predictions due to various choices of recoil scheme, evolution and splitting parameters. In a detailed comparison with experimental data from Drell-Yan lepton-pair production at the LHC we find that systematic uncertainties are relatively small. The only exception arises from the choice of recoil momentum, leading to sizable uncertainties in some regions of phase space. Driven by the comparison with data, we argue that for generic LHC Drell-Yan plus multi-jet events, the appropriate choice is a recoil vector that includes all final-state particles.

We further highlighted the capabilities of the ALARIC algorithm by comparing its predictions with an indicative range of relevant observables, in particular the jet multiplicities in Drell-Yan lepton pair production at the LHC. We also presented the first predictions for inclusive jet and di-jet production. We find that the quality of the description of experimental data from the LHC is in line with the current formal precision of the simulation.

In the near future, we will implement a next-to-leading order matching procedure, and extend the leading-order merging to next-to-leading order precision. This will allow us to obtain state-of-the art predictions for LHC measurements using the ALARIC algorithm.

ACKNOWLEDGMENTS

We thank Robert Szafron for discussions on the treatment of sub-leading power corrections in SCET. This research was supported by the Fermi National Accelerator Laboratory (Fermilab), a U.S. Department of Energy, Office of Science, HEP User Facility. Fermilab is managed by Fermi Research Alliance, LLC (FRA), acting under Contract No. DE-AC02-07CH11359. This research used the Fermilab Wilson Institutional Cluster for code development, testing, validation and production. We are grateful to James Simone for his support. F.K. gratefully acknowledges funding as Royal Society Wolfson Research fellow. F.K. and D.R. are supported by the STFC under grant agreement ST/P006744/1.

-
- [1] R. K. Ellis *et al.*, (2019), arXiv:1910.11775 [hep-ex].
 - [2] M. Narain *et al.*, (2022), arXiv:2211.11084 [hep-ex].
 - [3] J. N. Butler *et al.*, (2023), 10.2172/1922503.
 - [4] A. Buckley *et al.*, Phys. Rept. **504**, 145 (2011), arXiv:1101.2599 [hep-ph].
 - [5] J. M. Campbell *et al.*, in *2022 Snowmass Summer Study* (2022) arXiv:2203.11110 [hep-ph].
 - [6] B. R. Webber, Nucl. Phys. **B238**, 492 (1984).
 - [7] M. Bengtsson, T. Sjöstrand, and M. van Zijl, Z. Phys. **C32**, 67 (1986).
 - [8] M. Bengtsson and T. Sjöstrand, Nucl. Phys. **B289**, 810 (1987).
 - [9] G. Marchesini and B. R. Webber, Nucl. Phys. **B310**, 461 (1988).
 - [10] J. C. Collins, Nucl.Phys. **B304**, 794 (1988).
 - [11] I. Knowles, Nucl.Phys. **B304**, 767 (1988).
 - [12] I. Knowles, Nucl.Phys. **B310**, 571 (1988).
 - [13] I. Knowles, Comput.Phys.Commun. **58**, 271 (1990).
 - [14] S. Frixione and B. R. Webber, JHEP **06**, 029 (2002), hep-ph/0204244.
 - [15] P. Nason, JHEP **11**, 040 (2004), hep-ph/0409146.
 - [16] S. Frixione, P. Nason, and C. Oleari, JHEP **11**, 070 (2007), arXiv:0709.2092 [hep-ph].
 - [17] S. Alioli, P. Nason, C. Oleari, and E. Re, JHEP **06**, 043 (2010), arXiv:1002.2581 [hep-ph].
 - [18] S. Höche, F. Krauss, M. Schönherr, and F. Siegert, JHEP **04**, 024 (2011), arXiv:1008.5399 [hep-ph].
 - [19] S. Höche, F. Krauss, M. Schönherr, and F. Siegert, JHEP **09**, 049 (2012), arXiv:1111.1220 [hep-ph].
 - [20] J. Alwall, R. Frederix, S. Frixione, V. Hirschi, F. Maltoni, O. Mattelaer, H.-S. Shao, T. Stelzer, P. Torrielli, and M. Zaro, JHEP **07**, 079 (2014), arXiv:1405.0301 [hep-ph].
 - [21] S. Catani, F. Krauss, R. Kuhn, and B. R. Webber, JHEP **11**, 063 (2001), hep-ph/0109231.
 - [22] L. Lönnblad, JHEP **05**, 046 (2002), hep-ph/0112284.
 - [23] F. Krauss, JHEP **08**, 015 (2002), hep-ph/0205283.
 - [24] J. Alwall *et al.*, Eur. Phys. J. **C53**, 473 (2008), arXiv:0706.2569 [hep-ph].

- [25] S. Höche, F. Krauss, S. Schumann, and F. Siegert, *JHEP* **05**, 053 (2009), arXiv:0903.1219 [hep-ph].
- [26] L. Lönnblad and S. Prestel, *JHEP* **03**, 019 (2012), arXiv:1109.4829 [hep-ph].
- [27] T. Gehrmann, S. Höche, F. Krauss, M. Schönherr, and F. Siegert, *JHEP* **01**, 144 (2013), arXiv:1207.5031 [hep-ph].
- [28] S. Höche, F. Krauss, M. Schönherr, and F. Siegert, *JHEP* **04**, 027 (2013), arXiv:1207.5030 [hep-ph].
- [29] R. Frederix and S. Frixione, *JHEP* **12**, 061 (2012), arXiv:1209.6215 [hep-ph].
- [30] L. Lönnblad and S. Prestel, *JHEP* **03**, 166 (2013), arXiv:1211.7278 [hep-ph].
- [31] S. Plätzer, *JHEP* **08**, 114 (2013), arXiv:1211.5467 [hep-ph].
- [32] A. H. Mueller, *Phys. Lett.* **B104**, 161 (1981).
- [33] B. I. Ermolaev and V. S. Fadin, *JETP Lett.* **33**, 269 (1981).
- [34] Y. L. Dokshitzer, V. S. Fadin, and V. A. Khoze, *Phys. Lett. B* **115**, 242 (1982).
- [35] Y. L. Dokshitzer, V. S. Fadin, and V. A. Khoze, *Z. Phys.* **C15**, 325 (1982).
- [36] Y. L. Dokshitzer, V. S. Fadin, and V. A. Khoze, *Z. Phys. C* **18**, 37 (1983).
- [37] A. Bassetto, M. Ciafaloni, G. Marchesini, and A. H. Mueller, *Nucl. Phys.* **B207**, 189 (1982).
- [38] B. Webber, *Ann. Rev. Nucl. Part. Sci.* **36**, 253 (1986).
- [39] M. Bengtsson and T. Sjöstrand, *Phys. Lett.* **B185**, 435 (1987).
- [40] M. Dasgupta and G. Salam, *Phys.Lett.* **B512**, 323 (2001), arXiv:hep-ph/0104277 [hep-ph].
- [41] G. Gustafson and U. Petterson, *Nucl. Phys.* **B306**, 746 (1988).
- [42] B. Andersson, G. Gustafson, and L. Lönnblad, *Nucl. Phys.* **B339**, 393 (1990).
- [43] L. Lönnblad, *Comput. Phys. Commun.* **71**, 15 (1992).
- [44] W. T. Giele, D. A. Kosower, and P. Z. Skands, *Phys. Rev.* **D84**, 054003 (2011), arXiv:1102.2126 [hep-ph].
- [45] N. Fischer, S. Prestel, M. Ritzmann, and P. Skands, *Eur. Phys. J. C* **76**, 589 (2016), arXiv:1605.06142 [hep-ph].
- [46] H. Brooks, C. T. Preuss, and P. Skands, *JHEP* **07**, 032 (2020), arXiv:2003.00702 [hep-ph].
- [47] H. Brooks, P. Skands, and R. Verheyen, *SciPost Phys.* **12**, 101 (2022), arXiv:2108.10786 [hep-ph].
- [48] J. M. Campbell, S. Höche, H. T. Li, C. T. Preuss, and P. Skands, *Phys. Lett. B* **836**, 137614 (2023), arXiv:2108.07133 [hep-ph].
- [49] Z. Nagy and D. E. Soper, *JHEP* **10**, 024 (2005), hep-ph/0503053.
- [50] Z. Nagy and D. E. Soper, (2006), hep-ph/0601021.
- [51] S. Schumann and F. Krauss, *JHEP* **03**, 038 (2008), arXiv:0709.1027 [hep-ph].
- [52] W. T. Giele, D. A. Kosower, and P. Z. Skands, *Phys. Rev.* **D78**, 014026 (2008), arXiv:0707.3652 [hep-ph].
- [53] S. Plätzer and S. Gieseke, *JHEP* **01**, 024 (2011), arXiv:0909.5593 [hep-ph].
- [54] S. Höche and S. Prestel, *Eur. Phys. J.* **C75**, 461 (2015), arXiv:1506.05057 [hep-ph].
- [55] B. Cabouat and T. Sjöstrand, *Eur. Phys. J.* **C78**, 226 (2018), arXiv:1710.00391 [hep-ph].
- [56] M. Dasgupta, F. A. Dreyer, K. Hamilton, P. F. Monni, and G. P. Salam, *JHEP* **09**, 033 (2018), [Erratum: *JHEP* 03, 083 (2020)], arXiv:1805.09327 [hep-ph].
- [57] M. Dasgupta, F. A. Dreyer, K. Hamilton, P. F. Monni, G. P. Salam, and G. Soyez, *Phys. Rev. Lett.* **125**, 052002 (2020), arXiv:2002.11114 [hep-ph].
- [58] G. Bewick, S. Ferrario Ravasio, P. Richardson, and M. H. Seymour, *JHEP* **04**, 019 (2020), arXiv:1904.11866 [hep-ph].
- [59] J. R. Forshaw, J. Holguin, and S. Plätzer, *JHEP* **09**, 014 (2020), arXiv:2003.06400 [hep-ph].
- [60] Z. Nagy and D. E. Soper, *Phys. Rev. D* **104**, 054049 (2021), arXiv:2011.04773 [hep-ph].
- [61] Z. Nagy and D. E. Soper, (2020), arXiv:2011.04777 [hep-ph].
- [62] M. van Beekveld, S. Ferrario Ravasio, G. P. Salam, A. Soto-Ontoso, G. Soyez, and R. Verheyen, *JHEP* **11**, 019 (2022), arXiv:2205.02237 [hep-ph].
- [63] F. Herren, S. Höche, F. Krauss, D. Reichelt, and M. Schoenherr, *JHEP* **10**, 091 (2023), arXiv:2208.06057 [hep-ph].
- [64] B. Assi and S. Höche, (2023), arXiv:2307.00728 [hep-ph].
- [65] C. T. Preuss, (2024), arXiv:2403.19452 [hep-ph].
- [66] G. Gustafson, *Nucl. Phys. B* **392**, 251 (1993).
- [67] Z. Nagy and D. E. Soper, *JHEP* **1206**, 044 (2012), arXiv:1202.4496 [hep-ph].
- [68] S. Plätzer and M. Sjöstrand, *JHEP* **07**, 042 (2012), arXiv:1201.0260 [hep-ph].
- [69] Z. Nagy and D. E. Soper, *JHEP* **06**, 097 (2014), arXiv:1401.6364 [hep-ph].
- [70] Z. Nagy and D. E. Soper, *JHEP* **07**, 119 (2015), arXiv:1501.00778 [hep-ph].
- [71] S. Plätzer, M. Sjöstrand, and J. Thorén, *JHEP* **11**, 009 (2018), arXiv:1808.00332 [hep-ph].
- [72] J. Isaacson and S. Prestel, *Phys. Rev. D* **99**, 014021 (2019), arXiv:1806.10102 [hep-ph].
- [73] Z. Nagy and D. E. Soper, *Phys. Rev. D* **100**, 074005 (2019), arXiv:1908.11420 [hep-ph].
- [74] Z. Nagy and D. E. Soper, *Phys. Rev. D* **99**, 054009 (2019), arXiv:1902.02105 [hep-ph].
- [75] J. R. Forshaw, J. Holguin, and S. Plätzer, *JHEP* **08**, 145 (2019), arXiv:1905.08686 [hep-ph].
- [76] S. Höche and D. Reichelt, *Phys. Rev. D* **104**, 034006 (2021), arXiv:2001.11492 [hep-ph].
- [77] M. De Angelis, J. R. Forshaw, and S. Plätzer, *Phys. Rev. Lett.* **126**, 112001 (2021), arXiv:2007.09648 [hep-ph].
- [78] J. Holguin, J. R. Forshaw, and S. Plätzer, *Eur. Phys. J. C* **81**, 364 (2021), arXiv:2011.15087 [hep-ph].
- [79] K. Hamilton, R. Medves, G. P. Salam, L. Scyboz, and G. Soyez, *JHEP* **03**, 041 (2021), arXiv:2011.10054 [hep-ph].
- [80] S. Höche, D. Reichelt, and F. Siegert, *JHEP* **01**, 118 (2018), arXiv:1711.03497 [hep-ph].
- [81] S. Jones and S. Kuttimalai, *JHEP* **02**, 176 (2018), arXiv:1711.03319 [hep-ph].
- [82] G. Aad *et al.* (ATLAS), *JHEP* **08**, 089 (2022), arXiv:2112.09588 [hep-ex].
- [83] A. Bassetto, M. Ciafaloni, and G. Marchesini, *Phys. Rept.* **100**, 201 (1983).
- [84] Y. L. Dokshitzer, *Sov. Phys. JETP* **46**, 641 (1977).

- [85] V. N. Gribov and L. N. Lipatov, *Sov. J. Nucl. Phys.* **15**, 438 (1972).
- [86] L. N. Lipatov, *Sov. J. Nucl. Phys.* **20**, 94 (1975).
- [87] G. Altarelli and G. Parisi, *Nucl. Phys.* **B126**, 298 (1977).
- [88] S. Catani, S. Dittmaier, and Z. Trocsanyi, *Phys. Lett. B* **500**, 149 (2001), hep-ph/0011222.
- [89] S. Catani, S. Dittmaier, M. H. Seymour, and Z. Trocsanyi, *Nucl. Phys.* **B627**, 189 (2002), hep-ph/0201036.
- [90] F. E. Low, *Phys. Rev.* **110**, 974 (1958).
- [91] T. H. Burnett and N. M. Kroll, *Phys. Rev. Lett.* **20**, 86 (1968).
- [92] V. Del Duca, *Nucl. Phys. B* **345**, 369 (1990).
- [93] Y. L. Dokshitzer, G. Marchesini, and G. P. Salam, *Phys. Lett. B* **634**, 504 (2006), arXiv:hep-ph/0511302.
- [94] S. Catani and M. Grazzini, *Nucl. Phys. B* **570**, 287 (2000), arXiv:hep-ph/9908523.
- [95] V. N. Gribov and L. N. Lipatov, *Sov. J. Nucl. Phys.* **15**, 675 (1972).
- [96] S. Catani and M. H. Seymour, *Nucl. Phys.* **B485**, 291 (1997), hep-ph/9605323.
- [97] J. André and T. Sjöstrand, *Phys. Rev. D* **57**, 5767 (1998), arXiv:hep-ph/9708390.
- [98] D. Amati, A. Bassetto, M. Ciafaloni, G. Marchesini, and G. Veneziano, *Nucl. Phys.* **B173**, 429 (1980).
- [99] S. Catani, B. R. Webber, and G. Marchesini, *Nucl. Phys.* **B349**, 635 (1991).
- [100] T. Gleisberg, S. Höche, F. Krauss, A. Schälicke, S. Schumann, and J. Winter, *JHEP* **02**, 056 (2004), hep-ph/0311263.
- [101] T. Gleisberg, S. Höche, F. Krauss, M. Schönherr, S. Schumann, F. Siegert, and J. Winter, *JHEP* **02**, 007 (2009), arXiv:0811.4622 [hep-ph].
- [102] E. Bothmann *et al.* (Sherpa), *SciPost Phys.* **7**, 034 (2019), arXiv:1905.09127 [hep-ph].
- [103] A. Buckley *et al.*, *Comput.Phys.Commun.* **184**, 2803 (2013), arXiv:1003.0694 [hep-ph].
- [104] G. Aad *et al.* (ATLAS), *Phys.Lett.* **B720**, 32 (2013), arXiv:1211.6899 [hep-ex].
- [105] G. Aad *et al.* (ATLAS), *JHEP* **09**, 145 (2014), arXiv:1406.3660 [hep-ex].
- [106] V. M. Abazov *et al.* (D0), *Phys. Rev. Lett.* **106**, 122001 (2011), arXiv:1010.0262 [hep-ex].
- [107] G. Aad *et al.* (ATLAS), *Eur. Phys. J. C* **80**, 616 (2020), arXiv:1912.02844 [hep-ex].
- [108] G. Aad *et al.* (ATLAS), *JHEP* **07**, 032 (2013), arXiv:1304.7098 [hep-ex].
- [109] S. Chatrchyan *et al.* (CMS), *Phys. Lett. B* **722**, 238 (2013), arXiv:1301.1646 [hep-ex].
- [110] M. Cacciari, G. P. Salam, and G. Soyez, *JHEP* **04**, 063 (2008), arXiv:0802.1189 [hep-ph].
- [111] T. Neumann and J. Campbell, *Phys. Rev. D* **107**, L011506 (2023), arXiv:2207.07056 [hep-ph].
- [112] A. Banfi, G. P. Salam, and G. Zanderighi, *JHEP* **06**, 038 (2010), arXiv:1001.4082 [hep-ph].
- [113] V. Khachatryan *et al.* (CMS), *Eur. Phys. J. C* **76**, 451 (2016), arXiv:1605.04436 [hep-ex].
- [114] C. Bierlich *et al.*, *SciPost Phys. Codeb.* **2022**, 8 (2022), arXiv:2203.11601 [hep-ph].
- [115] T. Sjöstrand and M. van Zijl, *Phys. Rev. D* **36**, 2019 (1987).
- [116] G. Aad *et al.* (ATLAS), *Eur. Phys. J. C* **71**, 1763 (2011), arXiv:1107.2092 [hep-ex].
- [117] S. Chatrchyan *et al.* (CMS), *Phys. Lett. B* **702**, 336 (2011), arXiv:1106.0647 [hep-ex].
- [118] G. Aad *et al.* (ATLAS), *Eur. Phys. J. C* **74**, 3117 (2014), arXiv:1407.5756 [hep-ex].
- [119] A. Tumasyan *et al.* (CMS), *JHEP* **01**, 188 (2022), arXiv:2109.03340 [hep-ex].
- [120] S. Caletti, O. Fedkevych, S. Marzani, D. Reichelt, S. Schumann, G. Soyez, and V. Theeuwes, *JHEP* **07**, 076 (2021), arXiv:2104.06920 [hep-ph].
- [121] D. Reichelt, S. Caletti, O. Fedkevych, S. Marzani, S. Schumann, and G. Soyez, *JHEP* **03**, 131 (2022), arXiv:2112.09545 [hep-ph].
- [122] A. J. Larkoski, J. Thaler, and W. J. Waalewijn, *JHEP* **11**, 129 (2014), arXiv:1408.3122 [hep-ph].
- [123] J. R. Andersen *et al.*, *9th Les Houches Workshop on Physics at TeV Colliders*, (2016), arXiv:1605.04692 [hep-ph].